



Glass-in-glass infiltration for 3D micro-optical composite components

ENRICO CASAMENTI,^{1,*} Gözden Torun,¹ Luciano Borasi,² Maxime Lautenbacher,¹ Mathieu Bertrand,³ Jérôme Faist,³ Andreas Mortensen,² and Yves Bellouard¹

¹Galatea Laboratory, IEM, Ecole Polytechnique Fédérale de Lausanne (EPFL), CH – 2000 Neuchâtel, Switzerland

²Laboratory of Mechanical Metallurgy, IMX, Ecole Polytechnique Fédérale de Lausanne (EPFL), CH – 1015 Lausanne, Switzerland

³Institute for Quantum Electronics, D-PHYS, ETH Zurich, CH – 8093 Zurich, Switzerland

*enrico.casamenti@epfl.ch

Abstract: Chalcogenide glass exhibits a wide transmission window in the infrared range, a high refractive index, and nonlinear optical properties; however, due to its poor mechanical properties and low chemical and environmental stability, producing three-dimensional microstructures of chalcogenide glass remains a challenge. Here, we combine the fabrication of arbitrarily shaped three-dimensional cavities within fused silica molds by means of femtosecond laser-assisted chemical etching with the pressure-assisted infiltration of a chalcogenide glass into the resulting carved silica mold structures. This process enables the fabrication of 3D, geometrically complex, chalcogenide-silica micro-glass composites. The resulting products feature a high refractive index contrast that enables total-internal-reflection guiding and an optical quality roughness level suited for applications in the infrared.

© 2022 Optica Publishing Group under the terms of the [Optica Open Access Publishing Agreement](#)

1. Introduction

The use of glass has been ubiquitous in optics since the dawn of the discipline: the combination of two glass with different properties into a single product has been practiced since the late XVIIIth century, both for decorative and scientific purposes. Continuous progress and research in glass science have led to the discovery of a broad variety of glass compositions and formulations covering a wide range of useful physical properties, e.g. transparency spectral window, chromatic dispersion, linear and non-linear refractive indices, surface scratch resistance, brittleness, chemical stability, etc., which have found countless applications in optics and beyond. Yet, as a result of this broad spectrum of properties, great variability in processing methods and their outcomes remains. Specifically, forming glass in complex shapes at the microscale remains challenging, in particular for infrared glass that are notably often fragile and difficult to process.

Combining different glass into one product has been of great interest in early glass craftwork for decorative purposes. Venetians refined and magnified ancient work developing processes such as the *murrina* and the *millefiori*, which remain even nowadays iconic references for ornamental glass manufacturing [1–3]. In parallel, late-XVIIIth century scientific glasswork led to the discovery of achromatic optics ('Crown-Flint' doublets) [4]. The ability to produce freefrom glass-glass composites by novel methods capable of greater geometrical freedom of design than is currently possible could trigger optical component innovations with functionalities that leverage the individual physical properties of its basic constituents. This would offer novel design opportunities, in particular for further miniaturization and system integration. We present here a process allowing for the three-dimensional micro-scale integration of two glass with radically different physical properties. We illustrate this generic concept with free-form chalcogenide glass structures embedded in a fused silica matrix.

Chalcogenide glass has attracted much attention in the last few decades because their exceptionally wide optical transmission window in the infrared and their high nonlinear refractive index [5], for both passive [6,7] and active [8,9] photonic applications. Unfortunately, due to their poor mechanical properties and weak chemical and environmental stability [10,11], three-dimensional structuring, integration, and packaging of those glass remain challenging tasks. Current pathways to chalcogenide glass fabrication include the production of optical fibers and deposition processes. Chalcogenide glass fiber production was first reported in the 1980s [12] and continues, as such fibers have multiple applications, from sensing to telecommunications [5,13,14]. Photonic crystal fibers (PCFs) combining chalcogenide or tellurite glass into silica were produced by a pressure-infiltration technique, exploring both the process and optical properties of the resulting structures [15,16]. By this route, several centimeters long PCFs containing chalcogenide rods down to sub-micron diameter were manufactured [15–18]. Deposition processes such as chemical vapor deposition [19], physical vapor deposition followed by glass melting over etched silicon [20], sputtering [21], and pulsed laser deposition [22] are employed in applications for optical circuits, which require planar waveguides and components. Chalcogenide glass components such as lenses are currently fabricated by glass molding [23] and high-precision diamond-turning [24], restricting shapes to specific 3D geometries [25]. Recently, attempt to 3D print of chalcogenide using the fused-deposition technique applied to fiber preforms in As₂S₃ (one of the commercially available chalcogenides) has been reported [26–28]. This approach remains limited in resolution by the size of the filaments, which currently constrains designs to millimeter-scale geometries and introduces discontinuity between printed layers, which may be detrimental for certain optical applications.

The process that we present here is based on pressure-assisted infiltration of As₂S₃ chalcogenide glass into a fused silica micro-mold fabricated by femtosecond laser machining followed by chemical etching. This method enables the fabrication of arbitrary three-dimensional glass-in-glass elements while maintaining micrometric resolution and sub-micron roughness. The two constitutive materials, fused silica and chalcogenide, offer a high-index contrast combination, in geometries and size scales suited for geometrically complex 3D mid-infrared optics based on total internal reflection optical design principles. In addition to its specific optical properties, fused silica can be used as a mechanically and chemically resistant support and protection for chalcogenide microstructures, and may itself contain additional features of interest for further integration and packaging [29,30], such as waveguides [31] or flexures [32].

2. Experimental procedure

2.1. Infiltration process

The fabrication process, similarly to its metals infiltration counterpart [33,34], consists of two main steps. First, the fused silica micro-molds are machined using femtosecond laser modification followed by wet chemical etching (Fig. 1(A)-(B)), according to a process described elsewhere [35–37]. We use in the present work a Ytterbium-fiber amplifier laser emitting 270 fs pulses at a repetition rate of ~300 kHz, with a pulse energy of 220 nJ. The laser is focused to a measured optical waist of about ~2 μm using a 0.4-numerical aperture objective. The substrate used is UV-grade fused silica (Corning 7980 OF). Following laser exposure, the specimen is etched in a 5 wt% NaOH bath for several hours [37]. Then the micro-mold is positioned in a glass crucible with the chalcogenide glass As₂S₃ (IRG27, from Schott) to be infiltrated resting on top.

The crucible-glass combination is placed in a pressure infiltration furnace, and then brought to low vacuum (~ 0.02 mbar) while the temperature is raised to 600 °C (well above the transition temperature of IRG27 at 200 °C), according to values previously reported [16]. Thus, the chalcogenide is melted to a liquid form that covers the mold cavities (Fig. 1(C)). Note that, given that the chalcogenide glass As₂S₃ contains arsenic, it is important to prevent at this stage of the process any contamination of the furnace by arsenic that may have evaporated while the glass is

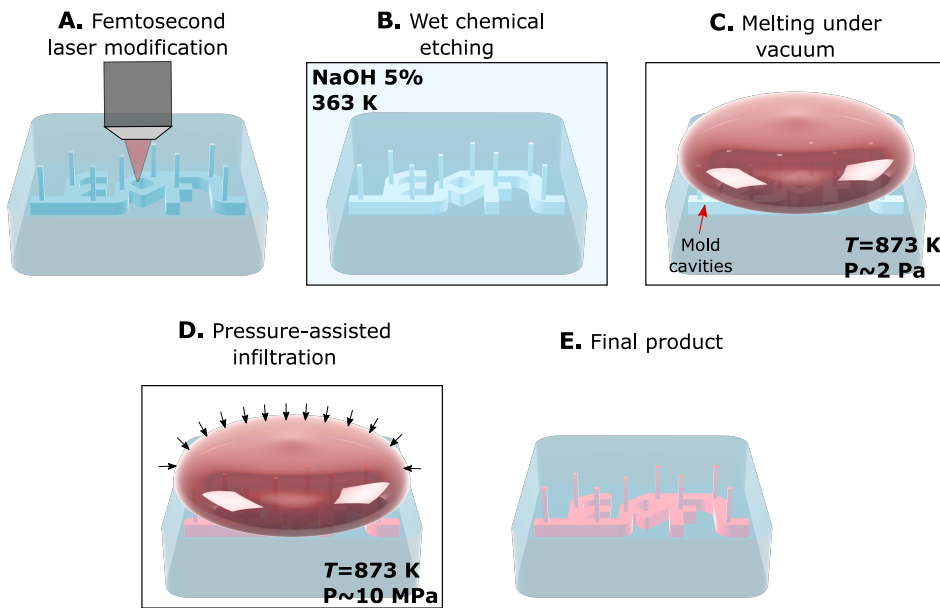


Fig. 1. Schematic of the micro-infiltration process. (A) A 3D pattern is inscribed in a fused silica substrate with a femtosecond laser. (B) The glass substrate is etched to remove the laser-irradiated regions. (C) The substrate is placed in a chamber with the glass to be infiltrated on top, the chamber is evacuated and the temperature is raised above the transition temperature of the infiltrant. (D) Pressurized inert gas is let into the chamber (but not mold cavities, which are sealed by the molten glass) and pushes the molten glass into the substrate cavities against capillary forces. (E) A final glass-in-glass composite product is obtained, shown here after removal of the remaining glass drop resting on top of the substrate.

molten. It is therefore advised to surround (as depicted in Fig. 1(C) and (D)) the molten glass with an inner enclosure within the pressure infiltration furnace, so as to prevent any transfer of arsenic to the furnace.

Then, to force the glass into the mold, a pressure of 10 MPa is applied hydrostatically with Argon gas leaked into the chamber, causing the molten chalcogenide glass to infiltrate the cavities underneath (Fig. 1(D)). Finally, the sample is cooled down while maintaining the pressure. After removing the excess chalcogenide by polishing, a final product combining 3D chalcogenide microstructures in fused silica is obtained (Fig. 1(E)). A post-processing annealing step is also implemented to minimize $-H$ and $-OH$ bonds and to ensure stress relaxation [38]. Namely, to obtain a high transmission and to avoid crystallization, the specimens are annealed in an inert atmosphere (i.e. nitrogen) at 150 °C for 1 hour using a heating and cooling rate of ~ 1 °C/min [38–40].

2.2. Material characterization

Optical micrographs are taken with a Hirox digital microscope KH-8700 (Tokyo, Japan) using the Köhler illumination method and, in the case of Fig. 4(E), with a standard linear polarimetry scheme. The samples are polished with diamond lapping films until an optical surface quality is obtained, then they are coated with carbon thin film for high-resolution imaging and elemental analysis with a field emission scanning electron microscope Zeiss SEM Gemini450 (Oberkochen, Germany) equipped with energy-dispersive x-ray spectroscopy (EDS). Images are obtained at 5 kV and elemental analysis is performed at 20 kV.

A Raman spectrometer, LabRam HR from Horiba (Kyoto, Japan), equipped with a 633 nm laser excitation source attenuated down to 4 mW (to prevent damaging the specimen) is used. The linearly polarized Raman laser beam is focused at the surface of the specimen using a 100x and 0.9 numerical aperture objective from Thorlabs (Newton, NJ, USA). Raman spectra at various points are collected at room temperature with an acquisition time of 30 seconds for each point.

Spectral transmission data in the visible and near-infrared spectrum (from 350 to 800 nm) are taken with a Perkin Elmer spectrometer Lambda 950 (Waltham, Massachusetts, USA). A mask with a hole of around $90 \times 90 \mu\text{m}^2$ is prepared in fused silica using the femtosecond laser machining plus etching process described above, and then coated with aluminum for broadband reflectance. For the measurement, the reference beam power is attenuated to 1%, to compensate for the presence of the mask and the ensuing effective drastic reduction of the beam size from the original 2 cm in diameter.

A CO laser (model C55 from Coherent, Santa Clara, California, USA) emitting at 5.55 μm is used to measure the transmission efficiency in the mid-infrared spectrum. The power transmitted is filtered with a bandpass filter (FB5500-500 from Thorlabs, Newton, NJ, USA) and is measured with a high sensitivity thermopile sensor (XLP12-3S-H2-D0 from Gentec-EO, Quebec, QC, Canada).

The light-guiding properties of the long channels in Fig. 2(C) are tested with an optical set-up comprising a quantum cascade laser (QCL) operating in continuous wave mode at 8.3 μm with 100 mW of output power, a set of two mid-IR lenses with anti-reflective coating with a focal length of 4 mm (C036TME-F from Thorlabs, Newton, NJ, USA) used for in and out coupling of the laser beam, a long wave IR camera (A400 from Teledyne FLIR, Wilsonville, OR, USA) to measure the radiation and scattered light, and a beam profiler working in the range from 2 to 16 μm (WinCamD-IR-BB from DataRay, Redding, CA, USA) to measure the beam profile of the out coupled light.

3. Results and discussion

Figure 2 displays optical images of structures produced with the presented process. Figure 2(A) shows a set of pillars with dimensions ranging from 30 to 150 μm laterally and from 400 to 500 μm in height. The “EPFL” logo in Fig. 2(B) demonstrates the production of complex geometries out of chalcogenide glass at the microscale, while the long channels in Fig. 2(C) show an aspect ratio (here defined as length over thickness) of around 80, thus demonstrating a structure that might be used as an infrared waveguide embedded in a fused silica substrate. Trapped gas bubbles found in the chalcogenide glass infiltrated PCFs [15–18] were not observed here. However, we note that structures infiltrated here are not as spectacularly long as those achieved in fiber infiltration and that the infiltration conditions are not the same. Namely, the mold is at constant temperature (i.e. no thermal gradient is present as was the case with the long PCFs) and the infiltration chamber is evacuated prior to melting and pressurization, so that there is no gas trapping in the present experiments. Cracks might on the other hand be present in the complex geometry samples of this work, given the changes in hue of the chalcogenide glass in Fig. 2(B). It should be mentioned that the darker lines visible in Fig. 2 A-B are typical surface texturing due to the laser machining followed by chemical etching of the glass mold and therefore likely not defects from the infiltration process. The roughness of the structures is defined by the femtosecond laser machining of the mold and depends chiefly on laser parameters and the writing strategy used. When those are optimized, an average roughness of about 100 nm can be achieved [37]. Therefore, the structures produced by the presented process can fulfill optical quality requirements for applications in the infrared.

The samples of Fig. 2(A) are characterized by performing both Raman and EDS to compare the pristine with the infiltrated glass. Raman analysis (Fig. 3(A)) shows spectra for the fused silica substrate (in blue), the infiltrated chalcogenide (in red), the pristine chalcogenide (in dark

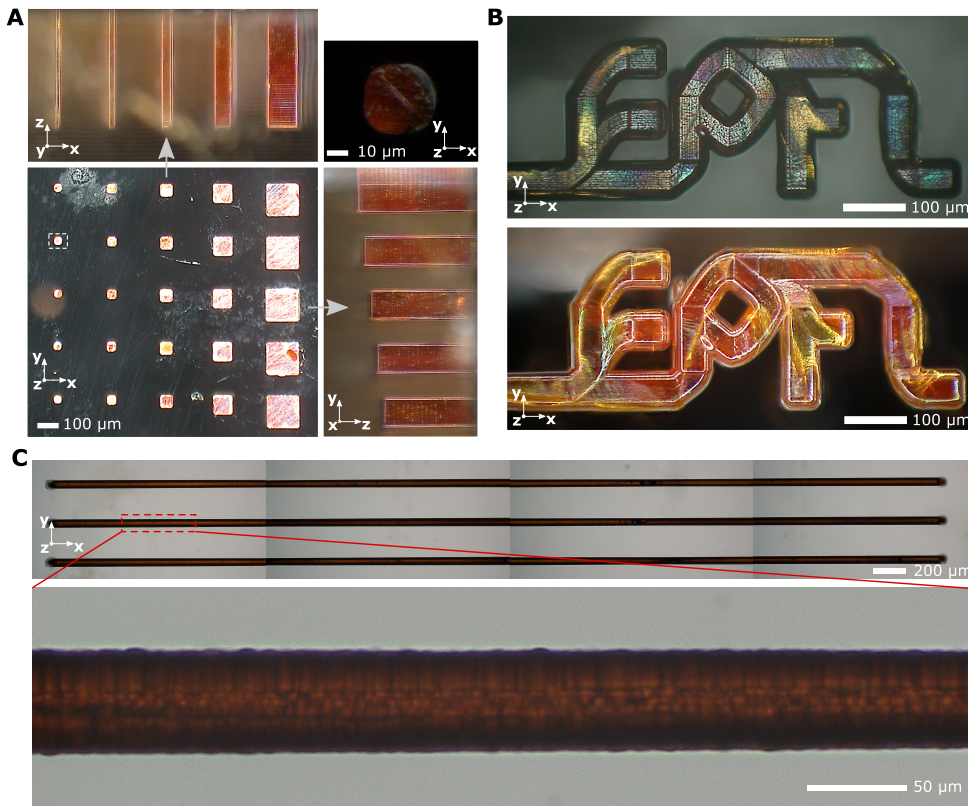


Fig. 2. Optical micrographs of different chalcogenide structures infiltrated into fused silica. (A) A set of pillars of different dimensions with a zoomed view (top right) of the pillar framed in the white dotted rectangle, representing the smallest cavity infiltrated in this work. The lateral view images are in scale with the related top view micrograph. (B) A complex 3D shape in dark and bright field illumination, and (C) overview (top) and magnification (bottom) of infiltrated channels 4 mm long and around 50 μm thick and wide (four micrographs are stitched together to form the figure).

grey), and the interface between fused silica and the infiltrated chalcogenide (in green). The Raman spectrum of the substrate matches with a typical Raman spectrum of fused silica. It shows the main band (ω_1), the symmetric stretching of the four-membered silicon-oxygen ring structure (D1), together with signatures of the three-membered silicon-oxygen ring structure (D2) and of the symmetric stretching mode of the Si-O-Si bridging bond in $\text{Si}(\text{O}_{1/2})_4$ tetrahedron network (ω_3) at 440 cm^{-1} , 490 cm^{-1} , 606 cm^{-1} , and 800 cm^{-1} , respectively [41,42]. For comparison with the unmodified glass, the intensity of the D2 peak is measured relative to the ω_3 peak intensity, which is known to remain constant with respect to the overall Raman intensity [43].

The structure of glassy As_2S_3 consists mainly of $\text{AsS}_{3/2}$ pyramidal units linked by As–S–As bridges. The main band at 345 cm^{-1} is assigned to the symmetric stretching vibrational mode of $\text{AsS}_{3/2}$ pyramids [44]. Weak bands at around 185 cm^{-1} , 228 cm^{-1} , and 475 cm^{-1} are associated with bending modes in As–As homopolar bonds within As_4S_4 clusters and S_8 rings, respectively [45].

The atomic structure and related properties of the chalcogenide glass depend on the fabrication history of the glass. As seen in Fig. 3(A), there is no structural modification observed between

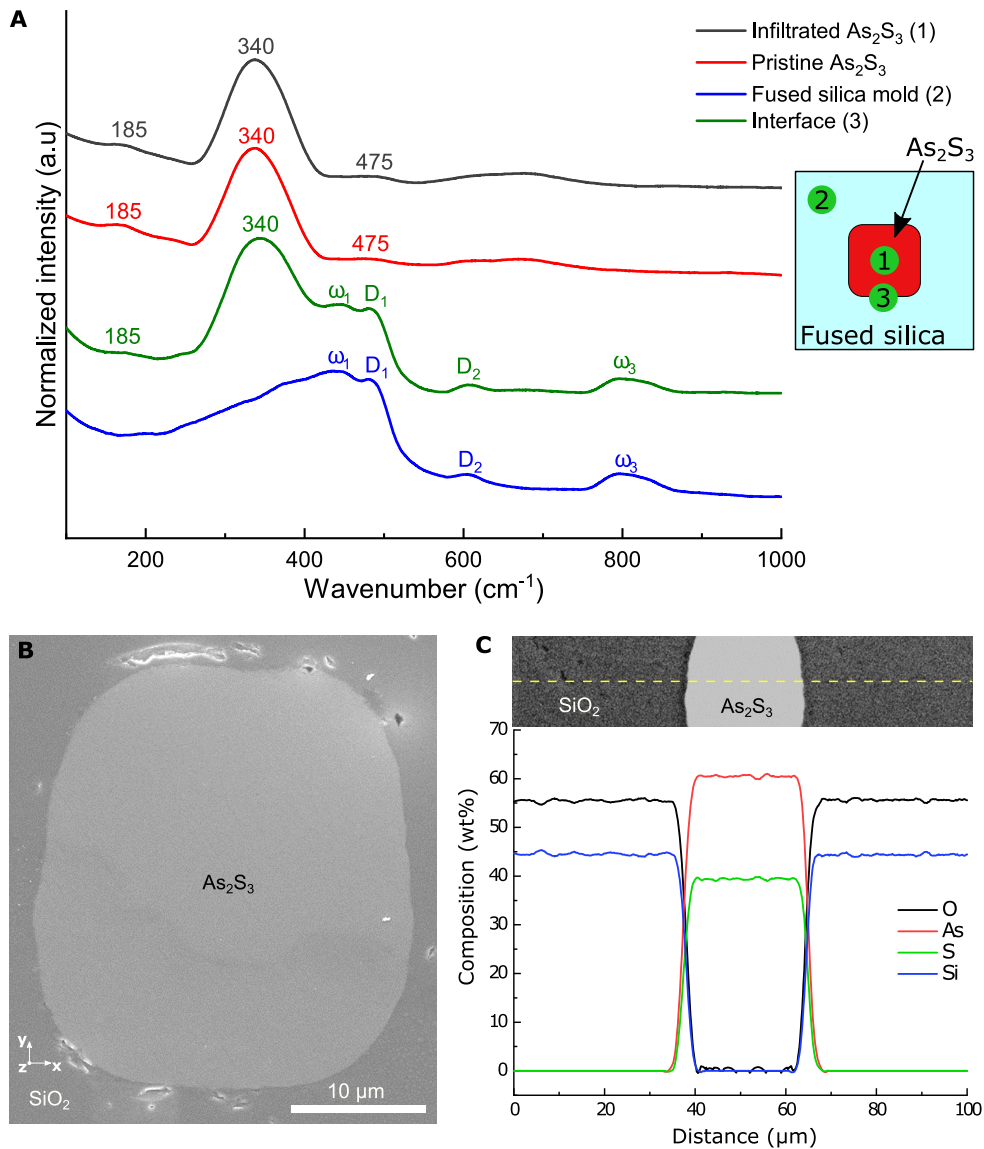


Fig. 3. (A) Raman spectra of fused silica mold (in blue), both pristine and infiltrated As_2S_3 chalcogenide (in dark grey and red, respectively), and at the interface between fused silica and infiltrated chalcogenide (in green). The inset shows a schematic representation of the measurements locations on the sample. (B) SEM micrograph of a cross-section of a chalcogenide filled channel in fused silica (the stain on the chalcogenide was caused by the acetone used before the SEM characterization and the particles on the surface are residues from polishing), and (C) EDS measurement of the chemical composition of mold and As_2S_3 after infiltration.

pristine As_2S_3 and the pressure-infiltrated As_2S_3 . This shows that the final product is a glassy material, similar to the raw material that was used for infiltration.

Finally, a Raman spectrum at the interface between the fused silica mold and the infiltrated chalcogenide structure is taken, with a goal to spot eventual oxygen and sulfur exchange. The sulfur oxygen vibrational modes were found in the literature as follows: broad bands at 928 cm^{-1} and 620 cm^{-1} due to symmetric and asymmetric stretching of S-O and symmetric bending modes of O-S-O, respectively [46]; two broad peaks at 310 cm^{-1} and 370 cm^{-1} for bending S-O vibrations [47,48]; molecular SO_2 at room temperature O-S-O at $530\text{--}570 \text{ cm}^{-1}$ [49]; and absorption bands at around 790 cm^{-1} and 800 cm^{-1} due to oxygen impurity in As_2S_x glass [50]. No evidence of S-O bonds is observed in the measured spectrum, which displays a blend of chalcogenide and fused silica characteristic peaks.

From the scanning electron micrograph in Fig. 3(B) of one of the finer infiltrated features of this work (see the leftmost column in Fig. 2(A)) one can conclude that an intimate, void-, crack-, and reaction-free, sharp interface is formed between the chalcogenide glass and fused silica, consistent with earlier investigations of As_2S_3 infiltration into fused silica [16]. The same structure as in Fig. 3(B) subjected to an energy dispersive x-ray spectroscopy analysis gives results shown in Fig. 3(C). The chemical composition measurement confirms that the present infiltration process induces no change in stoichiometry, for both the infiltrated chalcogenide glass and the fused silica mold. In particular, the composition of As_2S_3 is found as 61.0 wt% arsenic and 39.0 wt% sulfur, which (considering the atomic weight of the components) gives an atomic ratio of arsenic to sulfur of 2.3 with a negligible error of 0.15%. As for the Raman characterization, no evidence of species exchange between fused silica and chalcogenide is found. This suggests that there was no chemical interaction between the mold and the infiltrant. More advanced techniques such as transmission electron microscopy equipped with energy-dispersive X-ray spectroscopy (TEM-EDS), electron energy loss spectroscopy (EELS), or electron probe microanalysis (EPMA) could be used for higher accuracy measurements of eventual ion exchange.

After material characterization, the set of pillars shown in Fig. 2(A) is polished to expose both top and bottom surfaces. Then, a spectrum analyzer is used to compare the transmission spectrum of pristine versus infiltrated As_2S_3 . An ad-hoc mask is designed and machined in fused silica through femtosecond laser exposure followed by chemical etching, after which it is coated by sputtering with aluminum to obtain a broadband reflectance spectrum. The spectral transmission measurement is first calibrated with only the mask in place while attenuating the reference beam power to 1%. Then, optical quality polished windows of pristine fused silica and of As_2S_3 having the same thickness as the target sample are placed behind the mask and analyzed. Finally, the fused silica mold with As_2S_3 infiltrated pillars is tested under the same condition, i.e. with the mask positioned in front to let the light pass through only one specific pillar (see Fig. 4(B)-(D)) 500 μm -thick and about $80 \times 80 \mu\text{m}^2$ in cross-section. In addition, to test the transmission with a mid-IR source, a CO laser beam is focused first on the mask alone and then with the sample behind the mask. For precise measurement, the power is filtered with a bandpass filter around 5550 nm before measuring with a thermopile sensor with a sampling rate of 0.1 Hz for 5 minutes. The averaged results give an initial power through the mask of around 2.4 mW that is then reduced to 1.4 mW when the sample is in place, resulting in transmission efficiency of about 58%. The results are shown in Fig. 4(A).

In general, for the measured wavelengths, the infiltrated chalcogenide transmission spectrum follows the same trend as its pristine counterpart, albeit with a decrease in transmission of around 20%. We attribute the larger optical losses within the infiltrated sample to multiple factors, including the polished surface roughness, diffraction losses due to shape mismatch and/or alignment errors between the mask and the substrate, as well as the possible presence of micro-cracks or other small volume defects that cannot be totally excluded. Finally, the annealing conditions used here are probably different from those used by the glass manufacturer and it

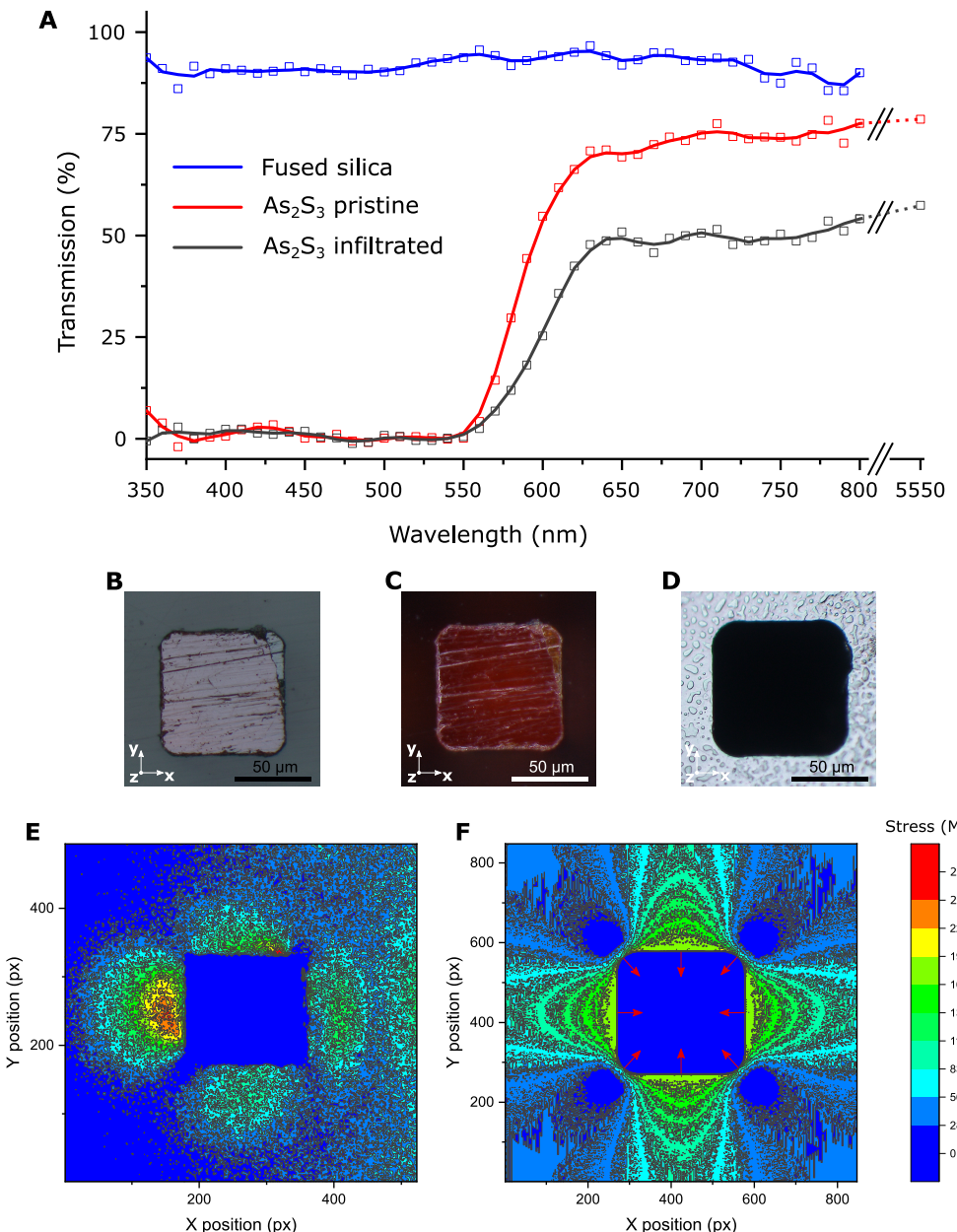


Fig. 4. (A) Spectral transmission measurements of fused silica together with both pristine and infiltrated As₂S₃. (B) and (C) optical micrographs of the chalcogenide infiltrated pillar (500 μm -thick and about $80 \times 80 \mu\text{m}^2$ in cross-section) viewed in reflection, and transmission, respectively. (D) optical micrograph of the hole in the aluminum-coated mask (the stains in the picture are an unexpected feature of the aluminum coating). (E) Colored map of an optical micrograph in cross-polarized illumination of the tested pillar. (F) Colored map of a FEA simulation of the stress distribution in the XY plane for the geometry considered in (E), with a uniform 110 MPa pressure applied as indicated by the red arrows.

is known that the optimization of such post-process operations is of great importance for the performance of chalcogenide glass. For example, by applying a two-step annealing (soft baking and hard baking), both optical and structural properties of As_2S_3 microstructures can be enhanced [51], and optimizing the annealing temperature increases the IR transmittance in As_2S_3 thin films [38].

Figure 4(E) shows the colored map of the pillar in a cross-polarization illumination setup, while Fig. 4(F) illustrates the simulated stress distribution using finite element analysis (FEA) within the same pillar. When subjected to mechanical stress, even isotropic materials such as fused silica become birefringent. Specifically, this stress-induced birefringence is linearly proportional to the stress state in the material. Here, we take advantage of this characteristic of the fused silica mold to *qualitatively* account for the presence of residual stress. Due to the photoelasticity effect, the brighter portions of the image in cross-polarizers indicate the presence of stress, with an intensity proportional to the light intensity. The presence of internal stresses within the glass near the interface confirms that, after infiltration, we obtain a composite with a strong, bonded interface between the two materials, as speculated from the SEM observations (see Fig. 3(B)). We note that this result differs from what was reported in [17,18], where a poor adhesion between As_2S_3 and silica was found. The reason for the difference remains unclear at this stage.

The presence of stress at the interface originates from the difference in thermal expansion coefficients (CTE) between the two materials, leading to a difference in shrinkage during solidification and cooling. In the simulation shown in Fig. 4(F), we estimate the difference in thermal shrinkage and the resulting level of stress by assuming a linear and isotropic behavior in the two materials, and finally, we apply the analytically computed stress uniformly (red arrows in Fig. 4(F)) on the finite element model of the fused silica mold to obtain the actual stress distribution in the plane perpendicular to the light propagation, i.e. XY. For the calculations, the coefficient of thermal expansion (CTE) and the Young modulus of chalcogenide glass are taken as $2.25 \cdot 10^{-5} \text{ K}^{-1}$ and 16.6 GPa (from [52]), respectively; while for fused silica we use $5.8 \cdot 10^{-7} \text{ K}^{-1}$ and 72.5 GPa (from Heraeus). The resulting thermal stress originating from the cooling and applied to the finite element model is estimated to be around 110 MPa.

For certain geometries and cooling conditions, depending on its intensity, this stress can result in the formation of cracks in the infiltrated structures, as visible in the complex geometry of Fig. 2(B) given the variations in the hue of the As_2S_3 geometry. This issue might be solved either by carefully optimizing the peak temperature and/or the cooling rate during infiltration or in post-processing annealing and/or by using a glass mold with a CTE similar to that of the infiltrant such as, for example, a borosilicate (i.e. $3.3 \cdot 10^{-6} \text{ K}^{-1}$, from Schott). It is worth noting that in case of a change in mold substrate, the infiltrant properties (as glass transition temperature and viscosity) and the process parameters (as temperature and pressure) define the minimum feature size that can be infiltrated. Therefore, although the parameters can be largely tuned, the ultimate constraints are set by the properties of the materials chosen – within the equipment capability. More information on modeling the pressure-assisted infiltration of chalcogenide in straight cylindrical holes can be found in [16–18].

As a proof-of-concept, we demonstrate the potential of this infiltration process by testing the long channels in Fig. 2(C) as mid-infrared waveguides. After fine-polishing the sample on both sides to expose both the waveguide's input and output (see schematic in Fig. 5(A)), a Gaussian beam emitted by a QCL laser operating at $8.3 \mu\text{m}$ is injected into the waveguide by the use of a high numerical aperture IR lens. An IR camera and a beam profiler are used to collect, respectively, thermal images of the set-up (Fig. 5(B)-(C)) and the collimated beam at the output of the mid-IR waveguide (Fig. 5(D)). The observation of a beam profile at the output of the waveguide suggests that the material quality and homogeneity in the waveguide is sufficient for guiding optical modes at this wavelength. This result is in line with the quasi-perfect material

properties match between infiltrated and pristine chalcogenide, and previous results reported in literature [16–18]. Noteworthy, the refractive indexes difference between the chalcogenide and the SiO₂ at 8.3 μm yields a very high numerical aperture (NA) waveguide. Therefore, with the optical element used for the output beam collimation, the NA of the lens limit the collection efficiency. The expected, theoretical beam-size on the beam profiler (assuming a 50 μm beam-size at the waveguide output) is of 2.4 mm where 0.65 mm is measured. The discrepancy is attributed to the high confinement of the beam in the waveguide due on one hand to the large refractive indexes difference, and on the other hand, to the sensitivity of the profiler and the collection optics not been optimized for the waveguide dimensions.

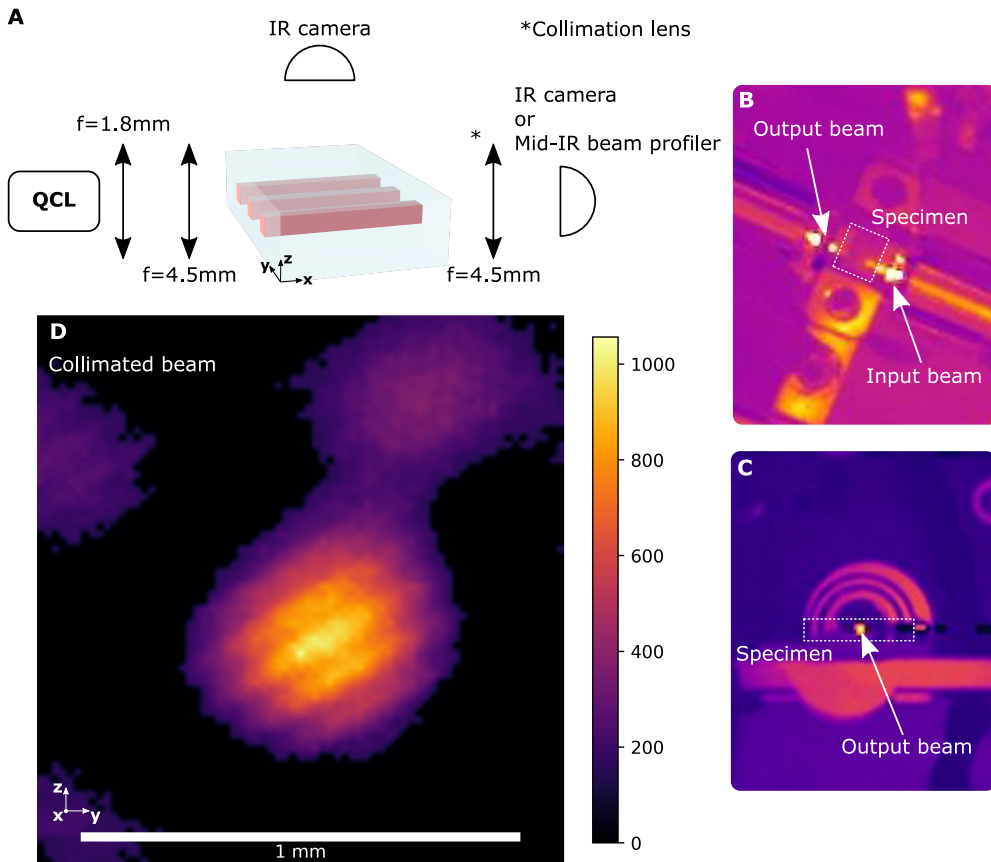


Fig. 5. Mid-IR waveguides testing. (A) Schematic of the setup used for testing the long channels of Fig. 2(C) after fine-polishing them on both sides (3.5 mm long and about 50 × 50 μm² in cross-section). Thermal images - top view (B) and lateral view (C) - of the setup showing the specimen under test and the beam input and output. (D) Collimated beam intensity profile image of the multimode waveguide output.

As shown by the samples presented above, the process enables the fabrication of three-dimensional chalcogenide structures in fused silica with micrometric precision. This innovation opens to innovative designs and further integration in the context of broadband photonics by offering a means to produce sub-mm components such as 3D waveguides, tapered or not, lenses, etc. all embedded in a robust silica substrate, that itself may contain additional features such as fluidic channels [36,53–57] or mechanical elements [29,32]. To cite one example, such components are particularly interesting for mid-IR spectroscopy applications.

Regarding resolution, the smallest structure produced in this study is about $30\text{ }\mu\text{m}$ in size; however, it is possible to push such limits further by tuning parameters such as the pressure used during infiltration or the viscosity of the infiltrant, which for glass depends greatly on temperature. As an illustration, with the same infiltration process, we have demonstrated infiltration of poorly wetting metals such as silver and gold into glass molds having features around $2\text{ }\mu\text{m}$ in size [33].

Finally, in this demonstration we employed As_2S_3 as a chalcogenide glass for its high glass-forming capability; however, we have not explored how high the glass-forming ability needs to be for the resulting infiltrated glass to always be amorphous in structures such as those of this work. We thus believe that there is scope to transpose the same concept to other glass systems, both within and outside the chalcogenide family, provided the following limitations are respected: (i) the infiltrant and the substrate are not to react mutually at the infiltration temperature, and (ii) the infiltrant must have a glass transition temperature lower than that of the substrate, such that there be sufficient contrast between the (low) infiltrant viscosity and that of the (solid) mold to be infiltrated.

4. Conclusion and outlook

In summary, we introduce a manufacturing technique by which one can fabricate microscale 3D chalcogenide microstructures embedded in fused silica. The process starts by carving a three-dimensional interconnected pattern into a fused silica mold using femtosecond laser exposure followed by chemical etching. The fabricated glass mold cavities are then filled with the second glass by pressure-assisted infiltration. As a proof of concept, As_2S_3 was employed; microstructural examination confirms the consistency of material properties before and after the infiltration.

The resulting silica-chalcogenide composites offer a high index contrast combination over a broad spectrum, with the silica mold acting as a mechanically and chemically resistant support and protection for the chalcogenide glass. This, together with the fine-scale 3D freeform capability of the presented manufacturing method, opens a wide range of broadband photonic applications for structures of the type presented here.

Acknowledgment. In this work, EC, GT, and LB implemented the experiments. EC designed and fabricated the substrates. EC and GT performed the optical characterization and prepared the draft manuscript. GT executed the material characterization. LB realized all the infiltrations and, as ML, contributed relevant preliminary experiments. MB did the IR waveguiding measurements with the help of Jakob Pretenthaler. AM and YB designed and supervised the research. All authors discussed and contributed to the article revisions. The Galatea laboratory acknowledges with gratitude the sponsoring of the chair by Richemont International SA. The Laboratory of Mechanical Metallurgy acknowledges funding of this work by internal laboratory funds provided by EPFL.

Disclosures. The authors declare no conflicts of interest related to this article.

Data availability. Data underlying the results presented in this paper may be obtained from the authors upon request.

References

1. V. Zanetti, *Piccola Guida Di Murano* (Libreria Filippi editrice, 1869).
2. A. Tosi and A. De Palma, eds., *La Memoria Del Vetro: Murano e l'arte Vetraria Nelle Storie Dei Suoi Maestri* (Marsilio : Scuola del vetro Abate Zanetti, 2006).
3. A. Pellatt, *Curiosities of Glass Making: With Details of the Processes and Productions of Ancient and Modern Ornamental Glass Manufacture* (TheClassics.us, 2012).
4. Maurice Daumas, *Les Instruments Scientifiques Aux XVIIe et XVIIIe Siecles*, 1st ed. (Presses Universitaires de France, Paris, 1953).
5. B. J. Eggleton, B. Luther-Davies, and K. Richardson, "Chalcogenide photonics," *Nat. Photonics* **5**(3), 141–148 (2011).
6. X. Zhang, B. Bureau, P. Lucas, C. Boussard-Pledel, and J. Lucas, "Glasses for Seeing Beyond Visible," *Chem. - Eur. J.* **14**(2), 432–442 (2008).
7. R. R. Gattass, R. Thapa, F. H. Kung, L. E. Busse, L. B. Shaw, and J. S. Sanghera, "Review of infrared fiber-based components," *Appl. Opt.* **54**(31), F25 (2015).

8. C. R. Petersen, U. Møller, I. Kubat, B. Zhou, S. Dupont, J. Ramsay, T. Benson, S. Sujecki, N. Abdel-Moneim, Z. Tang, D. Furniss, A. Seddon, and O. Bang, "Mid-infrared supercontinuum covering the 1.4–13.3 μm molecular fingerprint region using ultra-high NA chalcogenide step-index fibre," *Nat. Photonics* **8**(11), 830–834 (2014).
9. N. Abdellaoui, F. Starecki, C. Boussard-Pledel, Y. Shpotyuk, J.-L. Doualan, A. Braud, E. Baudet, P. Nemec, F. Cheviré, M. Dussauze, B. Bureau, P. Camy, and V. Nazabal, "Tb₃ + doped Ga 5 Ge 20 Sb 10 Se 65-x Te-x (x = 0–375) chalcogenide glasses and fibers for MWIR and LWIR emissions," *Opt. Mater. Express* **8**(9), 2887 (2018).
10. M. F. Churbanov, V. S. Shiryaev, V. V. Gerasimenko, A. A. Pushkin, I. V. Skripachev, G. E. Snopatin, and V. G. Plotnichenko, "Stability of the Optical and Mechanical Properties of Chalcogenide Fibers," *Inorg. Mater.* **38**(10), 1063–1068 (2002).
11. O. Mouawad, C. Strutynski, J. Picot-Clément, F. Désévédavy, G. Gadret, J.-C. Jules, and F. Smektala, "Optical aging behaviour naturally induced on As₂S₃ microstructured optical fibres," *Opt. Mater. Express* **4**(10), 2190 (2014).
12. T. Miyashita and Y. Terunuma, "Optical Transmission Loss of As-S Glass Fiber in 1.0–5.5 μm Wavelength Region," *Jpn. J. Appl. Phys.* **21**(Part 2, No. 2), L75–L76 (1982).
13. M. Asobe, T. Kanamori, and K. Kubodera, "Ultrafast all-optical switching using highly nonlinear chalcogenide glass fiber," *IEEE Photonics Technol. Lett.* **4**(4), 362–365 (1992).
14. J. Zhu, T. M. Horning, M. Zohrabi, W. Park, and J. T. Gopinath, "Photo-induced writing and erasing of gratings in As₂S₃ chalcogenide microresonators," *Optica* **7**(11), 1645 (2020).
15. M. A. Schmidt, N. Granzow, N. Da, M. Peng, L. Wondraczek, and P. St. J. Russell, "All-solid bandgap guiding in tellurite-filled silica photonic crystal fibers," *Opt. Lett.* **34**(13), 1946 (2009).
16. N. Da, L. Wondraczek, M. A. Schmidt, N. Granzow, and P. St. J. Russell, "High index-contrast all-solid photonic crystal fibers by pressure-assisted melt infiltration of silica matrices," *J. Non-Cryst. Solids* **356**(35–36), 1829–1836 (2010).
17. J. Kobelke, R. Spittel, D. Hoh, K. Schuster, A. Schwuchow, F. Jahn, F. Just, C. Segel, A. Hartung, J. Kirchhof, and H. Bartelt, "Preparation and characterization of microstructured silica holey fibers filled with high-index glasses," in F. Baldini, J. Homola, R. A. Lieberman, and K. Kalli, eds. (2011), p. 80732F.
18. R. Spittel, J. Kobelke, D. Hoh, F. Just, K. Schuster, A. Schwuchow, F. Jahn, J. Kirchhof, M. Jäger, and H. Bartelt, "Arsenic chalcogenide filled photonic crystal fibers," *J. Non-Cryst. Solids* **377**, 231–235 (2013).
19. C. C. Huang, D. W. Hewak, and J. V. Badding, "Deposition and characterization of germanium sulphide glass planar waveguides," *Opt. Express* **12**(11), 2501 (2004).
20. S. Serna, H. Lin, C. Alonso-Ramos, C. Lafforgue, X. Le Roux, K. A. Richardson, E. Cassan, N. Dubreuil, J. Hu, and L. Vivien, "Engineering third-order optical nonlinearities in hybrid chalcogenide-on-silicon platform," *Opt. Lett.* **44**(20), 5009 (2019).
21. W. C. Tan, M. E. Solmaz, J. Gardner, R. Atkins, and C. Madsen, "Optical characterization of a-As₂S₃ thin films prepared by magnetron sputtering," *J. Appl. Phys.* **107**(3), 033524 (2010).
22. K. E. Youden, T. Grevatt, R. W. Eason, H. N. Rutt, R. S. Deol, and G. Wylangowski, "Pulsed laser deposition of Ga-La-S chalcogenide glass thin film optical waveguides," *Appl. Phys. Lett.* **63**(12), 1601–1603 (1993).
23. X. H. Zhang, Y. Guimond, and Y. Bellec, "Production of complex chalcogenide glass optics by molding for thermal imaging," *J. Non-Cryst. Solids* **326–327**, 519–523 (2003).
24. J. D. Owen, M. A. Davies, D. Schmidt, and E. H. Urruti, "On the ultra-precision diamond machining of chalcogenide glass," *CIRP Ann.* **64**(1), 113–116 (2015).
25. S. Saini, K. Kritika, D. Devvrat, and M. D. Sharma, "Survey of chalcogenide glasses for engineering applications," *Mater. Today: Proc.* **45**, 5523–5528 (2021).
26. E. Baudet, Y. Ledemi, P. Larochelle, S. Morency, and Y. Messaddeq, "3D-printing of arsenic sulfide chalcogenide glasses," *Opt. Mater. Express* **9**(5), 2307 (2019).
27. J. Carcreff, F. Cheviré, E. Galdo, R. Lebullenenger, A. Gautier, J. L. Adam, D. L. Coq, L. Brilland, R. Chahal, G. Renversez, and J. Troles, "Mid-infrared hollow core fiber drawn from a 3D printed chalcogenide glass preform," *Opt. Mater. Express* **11**(1), 198 (2021).
28. J. Carcreff, F. Cheviré, R. Lebullenenger, A. Gautier, R. Chahal, J. L. Adam, L. Calvez, L. Brilland, E. Galdo, D. Le Coq, G. Renversez, and J. Troles, "Investigation on Chalcogenide Glass Additive Manufacturing for Shaping Mid-infrared Optical Components and Microstructured Optical Fibers," *Crystals* **11**(3), 228 (2021).
29. Y. Bellouard, A. A. Said, and P. Bado, "Integrating optics and micro-mechanics in a single substrate: a step toward monolithic integration in fused silica," *Opt. Express* **13**(17), 6635 (2005).
30. S. I. Nazir and Y. Bellouard, "Contactless Optical Packaging Concept for Laser to Fiber Coupling," *IEEE Trans. Compon., Packag. Manufact. Technol.* **11**(6), 1035–1043 (2021).
31. K. M. Davis, K. Miura, N. Sugimoto, and K. Hirao, "Writing waveguides in glass with a femtosecond laser," *Opt. Lett.* **21**(21), 1729 (1996).
32. V. Tielen and Y. Bellouard, "Three-Dimensional Glass Monolithic Micro-Flexure Fabricated by Femtosecond Laser Exposure and Chemical Etching," *Micromachines* **5**(3), 697–710 (2014).
33. L. Borasi, E. Casamenti, R. Charvet, C. Dénéréaz, S. Pollonghini, L. Deillon, T. Yang, F. Ebrahim, A. Mortensen, and Y. Bellouard, "3D metal freeform micromanufacturing," *Journal of Manufacturing Processes* **68**, 867–876 (2021).
34. A. Mortensen, Y. Bellouard, R. Charvet, and C. Dénéréaz, "Small-scale metal castings, small-scale metal/transparent composite structures, and process to produce the same," U.S. patent US10821505B2 (3 November 2020).

35. A. Marcinkevičius, S. Juodkazis, M. Watanabe, M. Miwa, S. Matsuo, H. Misawa, and J. Nishii, "Femtosecond laser-assisted three-dimensional microfabrication in silica," *Opt. Lett.* **26**(5), 277 (2001).
36. Y. Bellouard, A. Said, M. Dugan, and P. Bado, "Fabrication of high-aspect ratio, micro-fluidic channels and tunnels using femtosecond laser pulses and chemical etching," *Opt. Express* **12**(10), 2120 (2004).
37. E. Casamenti, S. Pollonghini, and Y. Bellouard, "Few pulses femtosecond laser exposure for high efficiency 3D glass micromachining," *Opt. Express* **29**(22), 35054 (2021).
38. S. Song, J. Dua, and C. B. Arnold, "Influence of annealing conditions on the optical and structural properties of spin-coated As₂S₃ chalcogenide glass thin films," *Opt. Express* **18**(6), 5472 (2010).
39. R. P. Wang, S. J. Madden, C. J. Zha, A. V. Rode, and B. Luther-Davies, "Annealing induced phase transformations in amorphous As₂S₃ films," *J. Appl. Phys.* **100**(6), 063524 (2006).
40. H. Khan, S. Islam, P. K. Dwivedi, N. Dilawar, M. Husain, and M. Zulfequar, "Effect of Annealing Temperature on Optical and Structural Properties of Solution Processed As₂S₃ Chalcogenide Glass Films," *Mater. Today: Proc.* **21**, 2072–2078 (2020).
41. A. Pasquarello and R. Car, "Identification of Raman Defect Lines as Signatures of Ring Structures in Vitreous Silica," *Phys. Rev. Lett.* **80**(23), 5145–5147 (1998).
42. N. Shen, M. J. Matthews, S. Elhadj, P. E. Miller, A. J. Nelson, and J. Hamilton, "Correlating optical damage threshold with intrinsic defect populations in fused silica as a function of heat treatment temperature," *J. Phys. D: Appl. Phys.* **46**(16), 165305 (2013).
43. A. E. Geissberger and F. L. Galeener, "Raman studies of vitreous Si O₂ versus fictive temperature," *Phys. Rev. B* **28**(6), 3266–3271 (1983).
44. T. Wagner, S. O. Kasap, M. Vlcek, A. Sklenář, and A. Stronski, "Modulated-temperature differential scanning calorimetry and Raman spectroscopy studies of As_xS_{100-x} glasses," *J. Mater. Sci.* **33**(23), 5581–5588 (1998).
45. W. Li, S. Seal, C. Rivero, C. Lopez, K. Richardson, A. Pope, A. Schulte, S. Myneni, H. Jain, K. Antoine, and A. C. Miller, "Role of S/Se ratio in chemical bonding of As–S–Se glasses investigated by Raman, x-ray photoelectron, and extended x-ray absorption fine structure spectroscopies," *J. Appl. Phys.* **98**(5), 053503 (2005).
46. L. Mandrile, I. Cagnasso, L. Berta, A. M. Giovannozzi, M. Petrozziello, F. Pellegrino, A. Aspraudi, F. Durbiano, and A. M. Rossi, "Direct quantification of sulfur dioxide in wine by Surface Enhanced Raman Spectroscopy," *Food Chem.* **326**, 127009 (2020).
47. P. Bazylewski, R. Divigalpitiya, and G. Fanchini, "In situ Raman spectroscopy distinguishes between reversible and irreversible thiol modifications in L-cysteine," *RSC Adv.* **7**(5), 2964–2970 (2017).
48. C. Luo, E. Hu, K. J. Gaskell, X. Fan, T. Gao, C. Cui, S. Ghose, X.-Q. Yang, and C. Wang, "A chemically stabilized sulfur cathode for lean electrolyte lithium sulfur batteries," *Proc. Natl. Acad. Sci. U. S. A.* **117**(26), 14712–14720 (2020).
49. Y. Song, Z. Liu, H. Mao, R. J. Hemley, and D. R. Herschbach, "High-pressure vibrational spectroscopy of sulfur dioxide," *J. Chem. Phys.* **122**(17), 174511 (2005).
50. S. Tsuchihashi and Y. Kawamoto, "Properties and structure of glasses in the system As[JS]," *J. Non-Cryst. Solids* **5**(4), 286–305 (1971).
51. P. Sachan, R. Singh, P. K. Dwivedi, and A. Sharma, "Infrared microlenses and gratings of chalcogenide: confined self-organization in solution processed thin liquid films," *RSC Adv.* **8**(49), 27946–27955 (2018).
52. W. F. Glaze, D. H. Blackburn, J. S. Osmalov, D. Hubbard, and M. H. Black, "Properties of Arsenic Sulfide Glass," *J. RES. NATL. BUR. STAN.* **59**(2), 83 (1957).
53. Y. Cheng, K. Sugioka, and K. Midorikawa, "Microfluidic laser embedded in glass by three-dimensional femtosecond laser microprocessing," *Opt. Lett.* **29**(17), 2007 (2004).
54. C. Hnatovsky, R. S. Taylor, E. Simova, V. R. Bhardwaj, D. M. Rayner, and P. B. Corkum, "Polarization-selective etching in femtosecond laser-assisted microfluidic channel fabrication in fused silica," *Opt. Lett.* **30**(14), 1867 (2005).
55. T. N. Kim, K. Campbell, A. Groisman, D. Kleinfeld, and C. B. Schaffer, "Femtosecond laser-drilled capillary integrated into a microfluidic device," *Appl. Phys. Lett.* **86**(20), 201106 (2005).
56. K. Sugioka, Y. Cheng, and K. Midorikawa, "Three-dimensional micromachining of glass using femtosecond laser for lab-on-a-chip device manufacture," *Appl. Phys. A* **81**(1), 1–10 (2005).
57. V. Maselli, R. Osellame, G. Cerullo, R. Ramponi, P. Laporta, L. Magagnin, and P. L. Cavallotti, "Fabrication of long microchannels with circular cross section using astigmatically shaped femtosecond laser pulses and chemical etching," *Appl. Phys. Lett.* **88**(19), 191107 (2006).